Microstructure, tensile and fractographic behavior of friction stir welded joints AA6061 and AA2024

C. N. Vikas, N. Nagesha
Department of Industrial and Production Engineering, University B. D. T. College of Engineering, Davangere, Visvesvaraya Technological University, Belagavi, Karnataka India.
vicky_vickymech@yahoo.co.in, *https://orcid.org/0009-0003-8578-312X*
nnvebs@gmail.com, *https://orcid.org/0000-0001-9088-1734*

Manjunath Vatnalmath
Department of Mechanical Engineering, RNS Institute of Technology, Bangalore-566098, Visvesvaraya Technological University, Belagavi, Karnataka, India.
vmanjunathsit@gmail.com, *https://orcid.org/0000-0003-3138-9453*

N. SathyaNarayana
Department of Mechanical Engineering, Government Engineering college, Mosalehosalli – 573212, India
sathya.227me013@nitk.edu.in, *http://orcid.org/0009-0001-5754-2332*

ABSTRACT. The present study focused on the evaluation of critical influencing parameters of the FSW of AA6061-T6 and AA2024-T351 alloys. The materials properties of AA6061-T6 are heat-treatable alloys possessing properties of good resistance to corrosion, and AA 2024-T351 has superior strength, which is very important in load bearing section. The joining of these AA alloys will result in excellent mechanical qualities. Friction stir welding (FSW) is a very crucial joining method in the aerospace and automobile sector resolving most of the problems connected to the requirement of high-performance welded joints. In preference, this kind of joining has more advantages over common joining processes, such as less defects, no use of consumable electrodes, and it can be applicable in welding at any position. In this research, optimization of critical influencing input parameters was conducted using the L9 orthogonal array by the Taguchi method. Overall, there were 9 experimental trials after designing in the statistical software. The input process parameters selected for optimization are tool rotation speed (TRS), welding feed rate (WS) and tilt angle, which is maintained constant at zero degrees. The relative contribution percentages of the input variables to the optimized outputs (TRS and WS) were determined via ANOVA.

Citation: Vikas, C. N., Nagesha., N., Vatnalmath, M., SathyaNarayana, N., Microstructure, tensile and fractographic behavior of friction stir welded joints AA6061 and AA2024, Fracture and Structural Integrity, 77 (2026) 120-137.

Received: 26.02.2026
Accepted: 20.04.2026
Published: 21.04.2026
Issue: 07.2026

KEYWORDS. Aluminium 6061-T6, Aluminium 2024-T351, Taguchi method, Ultimate tensile strength, Hardness, Taper threaded pin profile

INTRODUCTION

FSW is an advanced solid-state joining process developed by The Welding Institute (TWI) in 1991 that has changed the way aluminium alloys have been welded, especially those that are thought to be difficult to have welded via conventional fusion welding methods. In FSW, a revolving tool is created of a non-consumable pin and shoulder designed so that they can be placed into abutting sides of two work pieces that need to be joined, and in turn advances the joining line. Frictional heating takes place between the tool and the two work pieces while they are stirred mechanically producing a plasticized zone. Once cooled, the stir zone becomes solid and forms a solid-state joint. [1][2]. Aluminium alloys are widely used in engineering applications because of lighter in weight, superior resistance to corrosion, and good formability. FSW is greatly adopted for various heat treatable aluminium alloys such as 6xxx and 2xxx due to its advantages over conventional fusion welding process [3]. AA 6061-T6 is a heat-treatable alloy consisting of Si and Mg as major alloying elements, exhibits good weld ability and resistance to corrosion. AA 2024-T351 is a high-strength Al-Cu alloy with extraordinary fatigue resistance, commonly used in aircraft structures and parts of automobile. The joining of dissimilar AA alloys presents significant difficulties arising from variation in their density, physical, chemical, and mechanical properties. Conventional welding processes often end up in defects such as hot cracking, porosity, and formation of brittle IMC's. FSW, the most widely used solid-state welding method, are used effectively to join dissimilar materials while significantly increases microstructure and mechanical properties required aerospace applications. FSW operates well below the melting temperature of the base materials, thereby avoiding fusion-connected defects [4,5,6]. The mechanical properties of welded joints are significantly affected by input process parameters including tool rotational speed (TRS), welding speed (WS), tool geometry, plunge depth and tilt angle. TRS affects the generation of heat and flow of material during welding, while welding speed determines the heat input per unit length of the weld. The pin profile has a significant role in material mixing and plastic deformation. Among various pin profiles, the taper threaded pin profile (TTPP) has demonstrated superior material flow characteristics and enhanced mechanical properties because of efficient material stirring and reduced welding forces [7][8]. Optimization of FSW input process parameters is essential to achieve joints with superior mechanical properties. Traditional experimental approaches involving one-factor-at-a-time methodology are time-consuming and expensive. Taguchi's design of experiments (DOE) provides a structured and efficient method to optimize input process parameters with a lesser amount of experiments. This method uses orthogonal arrays to study effects of multiple factors simultaneously and employs signal-to-noise (S/N) ratio analysis to decide optimal parameter combinations [9][10]. Several researchers have investigated the FSW of dissimilar AA alloys. Studies on joining AA 6061-T6 and AA 2024-T351 alloys have reported that suitable selection of input process parameters and tool placement considerably influences the microstructure and mechanical properties of the joints. The flow stress behavior of AA 6061-T6 and AA 2024-T351 alloys at higher temperatures differs considerably, with AA 2024 shows higher flow stress compared to AA 6061, which impacts material flow during welding [11][12]. Despite extensive research on FSW of aluminium alloys, there is limited comprehensive statistical evaluation specifically addressing the welding of AA 6061-T6 and AA 2024-T351 using taper threaded pin profile (TTPP) with systematic optimization through Taguchi methodology. This research focuses on filling this gap by conducting a comprehensive investigation of the influence of TRS and WS on the ultimate tensile strength (UTS) and hardness of dissimilar FSW joints.

MATERIALS AND METHODS

Selection of base materials

The aluminium alloys selected for this research work were AA 6061-T6 and AA 2024-T351 composition and mechanical properties are as shown in Tab. 1 and 2. Both materials were cut into size with measurements of 100 × 50 × 8 mm. AA 6061-T6 consist of Mg-Si-Fe particle which enhances the property of the alloy to medium-

strength heat-treatable alloy with extraordinary corrosion resistance and good weld ability. AA 2024-T351 is a high capacity al-cu alloy popularly used in critical load bearing applications because of its higher mechanical properties and fatigue resistance.

Alloy	Al	Cu	Mg	Si	Fe	Mn	Cr	Zn
AA 6061-T6	Balance	0.19	0.68	0.47	0.40	0.06	0.19	-
AA 2024-T351	Balance	3.80	1.20	0.50	0.50	0.30	0.10	-

Table 1: Base materials chemical composition (wt. %)

Alloy	UTS (MPa)	Yield Strength (MPa)	Elongation (%)	Hardness (VHN)
AA 6061-T6	310	278	12	107
AA 2024-T351	469	324	19	137

Table 2: Base materials Mechanical properties.

Tool material and geometry

The TTPP tool is manufactured using H13 steel. The tool was fabricated and TTPP is subjected to heat treatment. Later, the tool is dipped in the oil bath (for 3 days) to increase the strength of the weld tool. Two main constituents of tool are shoulder cylindrical in shape and a taper threaded pin profile (TTPP). The diameter of shoulder was made with the dimension of 24 mm, created to produce enough frictional heat and apply forging pressure to Weld the plasticized material. The pin had a taper threaded profile with a maximum diameter of 8 mm at the shoulder connection, tapering to a minimum diameter of 6 mm at the end of tool tip. The 1 mm thread pitch with right-hand threads the pin length was 7.8 mm, moderately lesser than the plate thickness to avoid contact between tool shoulder and backing plate.

Experimental setup and welding method

The full experiment was carried out in a specialized FSW machine with three axis movement control. The maximum spindle speed was 3000 rpm with a power rating of 7.5 kW. The work pieces were placed on a fixture. On the advancing side AA2024-T351 is placed. The welding of two alloys will be carried out based on the set of input parameter values, obtained by the MINITAB software. Work pieces are held tightly in a fixture without any vibration. Fig. 1 shows the fixture and FSW machine used in this experiment. Weld orientation was orthogonal to the plate rolling direction. The tool tilt angle was maintained at 0° throughout all experiments to ensure consistent forging action and material consolidation.

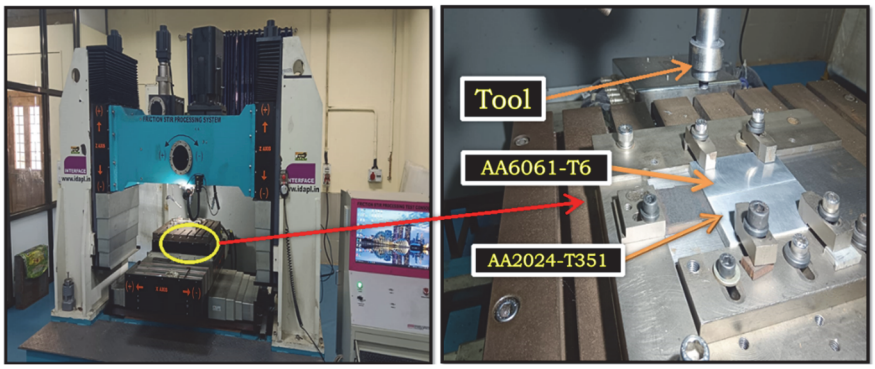

Figure 1: Friction stir welding setup.

Design of experiments - Taguchi L9 orthogonal array

The investigation was carried out based on the Taguchi L9 orthogonal array for the input parameters as shown in Tab. 3. A 9 trials 2-factor, 3-level orthogonal table was created by means of Taguchi's DOE, which is shown in Tab. 4. The table was generated by using the MINITAB 19 software. 0° tilt angle of tool was maintained constant all over the experiments.

Input Parameter	Symbol	Level -1	Level -2	Level -3
Tool Rotational Speed (TRS)(rpm)	A	600	700	800
Welding Feed Rate (WS) (mm/min)	B	25	30	35

Table 3: Input operating parameters and their levels.

Experiment No.	TRS (rpm)	WS (mm/min)
1	600	25
2	600	30
3	600	35
4	700	25
5	700	30
6	700	35
7	800	25
8	800	30
9	800	35

Table 4: L9 orthogonal array experimental design matrix.

Mechanical testing procedures: tensile testing

As shown in Fig. 2 and 3 for the tensile test specimen was taken from the welded joints orthogonal to the weld axis as per ASTM E8M-04 standards. The specimens were machined using Wire EDM to ensure precise dimensions and avoid thermal effects on microstructure at the edges. The gauge length was 25mm, width of 10 mm and thickness of 8 mm. Tensile testing was conducted on a UTM with a capacity of 200 kN at a speed of 1.5 mm/min.

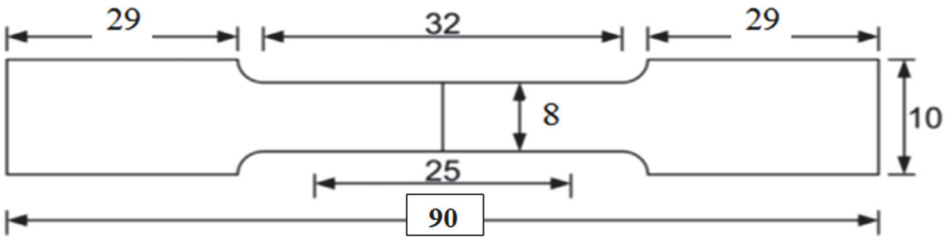

Figure 2: Tensile testing specimens as per ASTM E8M-04 standards.

Figure 3: Tensile specimens.

Mechanical testing procedures: hardness testing

Vickers micro hardness (VHN) measurements were carried out across the weld c/s to estimate the distribution of hardness in distinct zones of the welded joint. The welded samples were cut orthogonally to the welding direction, mounted in cold-setting epoxy resin, and polished using successive grades of SiC papers (from 320 to 2000 grit) followed by diamond paste polishing (3 μm and 1 μm) to achieve a mirror finish. Measurement of Hardness was conducted using a Vickers micro hardness tester with a load of 100 gf and a dwell time of 15 seconds. Hardness of welded joints were performed along the intermediate of the weld cross-section with an indentation spacing of 1 mm. On both sides of advancing and retreating edges multiple measurements were taken in the nugget zone, thermo-mechanically affected zone (TMAZ), heat-affected zone (HAZ), and base material regions.

RESULT AND DISCUSSIONS

Experimental results

Conducted experimental results for UTS and stir zone micro hardness for all 9 trials are tabulated in Tab. 5. The UTS values differ from 145 MPa for Sample 1 (600 rpm, 25 mm/min) to 230 MPa for Sample 9 (800 rpm, 35 mm/min), exhibiting the significant influence of input process parameters on joint strength. The hardness values in the nugget zone varied between 137 VHN and 154 VHN, with Sample-3 demonstrating the minimum hardness and Sample-1 showing the maximum hardness. Variation in hardness value at stir zone is as shown in Fig. 4.

Sample No.	Tool Speed (rpm)	Feed Rate (mm/min)	UTS (MPa)	Hardness (HV)
1	600	25	145	142
2	600	30	158	134
3	600	35	165	129
4	700	25	155	150
5	700	30	170	144
6	700	35	185	139
7	800	25	190	159
8	800	30	205	155
9	800	35	230	150

Table 5: Experimental results for UTS and hardness.

The results show that there is a common trend in the direction of increasing UTS with increasing TRS and WS. This action can be responsible for improved mixing of materials, refined grain structure, and improved consolidation at optimized input heat conditions. However, the hardness values showed highly complicated input process parameters, indicating contending mechanisms involving grain refinement, dissolution of precipitate, and thermal cycle exposure.

Signal-to-noise ratio analysis for UTS

S/N ratios for UTS were calculated using the larger-the-better criterion and are presented in Tab. 6. The S/N ratio's differ from 43.22 dB for Sample-1 to 47.23 dB for Sample-9, indicating considerable variation in performance of joint strength all over the specimen for different parameter combinations.

The main effects plot for S/N ratios of UTS is shown in Fig. 5. The plot indicates that both TRS and WS significantly influence the UTS of the welded joints. The S/N ratio increases progressively with increasing TRS from 600 rpm to 800 rpm, indicating improved joint strength at higher rotational speeds. Similarly, the S/N ratio increases with increasing WS from 25 mm/min to 35 mm/min. The analysis reveals the combinational optimal parameter set for maximum UTS is TRS of 800 rpm and WS of 35 mm/min. The highest UTS of 230 MPa is produced at this combination which represents

approximately 74% of the AA 6061-T6 base material strength and 49% of the AA 2024-T351 base material strength. The tensile strength increased with higher rotational speed can be linked to multiple causes. Higher rotational speeds generate higher frictional heat, resulting in increased temperatures and increased plastic flow of the material. This enhances better intermixing of the dissimilar alloys and reduces the tendency for defects, namely tunnel voids or insufficient bonding. Additionally, the dynamic recrystallization process is more active at higher temperatures, leading to finer grain structures in the SZ, which strengthens the joint according to the Hall-Petch relationship[15][16].In the parameter range experimented, the increased feed rate maintains beneficial thermal cycles that prevent abrupt grain growth and precipitate coarsening while ensuring sufficient material consolidation. The shorter heat cycle exposure at higher feed rates helps retain strengthening precipitates in the heat-treatable alloys [17][18].

Sample No.	TRS (rpm)	WS (mm/min)	UTS (MPa)	S/N Ratio (dB)
1	600	25	145	43.2274
2	600	30	158	43.9731
3	600	35	167	44.4543
4	700	25	163	44.2438
5	700	30	178	45.0084
6	700	35	185	45.3434
7	800	25	190	45.5751
8	800	30	205	46.2351
9	800	35	230	47.2346

Table 6: S/N ratios for UTS.

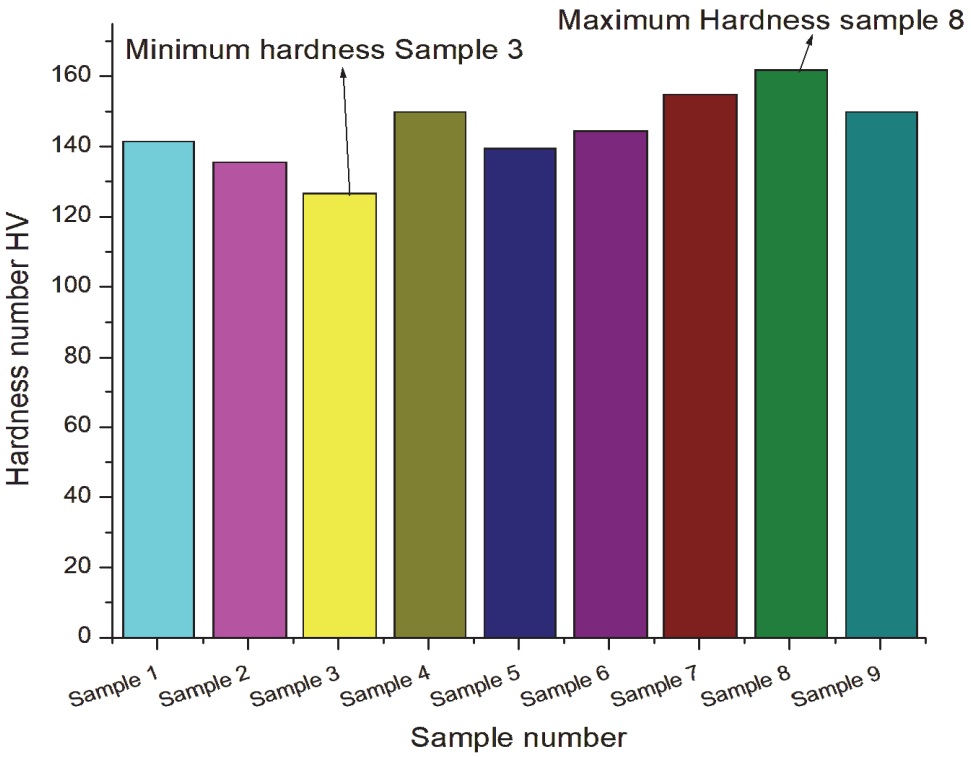

Figure 4: Stir zone hardness values.

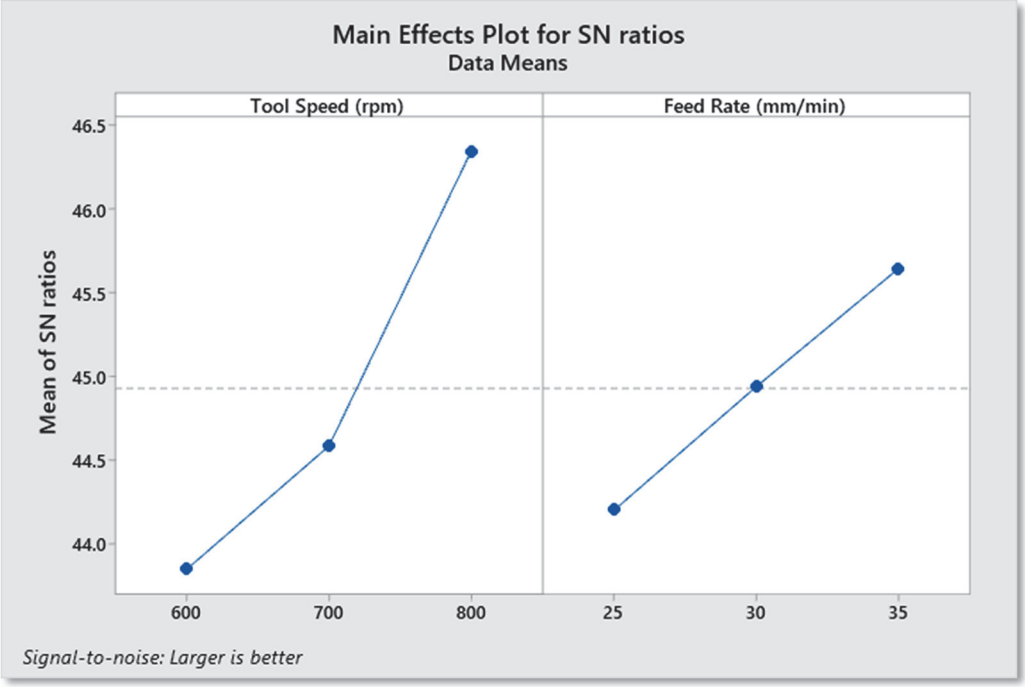

Figure 5: Main effects plot for S/N ratios of UTS.

S/N ratio analysis for micro hardness

The S/N ratios for hardness values at the SZ are tabulated in Tab. 7. The S/N ratios varies from 42.21 dB to 44.02 dB, showing comparatively smaller variation compared to UTS results.

Sample No.	TRS (rpm)	WS (mm/min)	Hardness (HV)	S/N Ratio (dB)
1	600	25	142	43.0458
2	600	30	134	42.5421
3	600	35	129	42.2118
4	700	25	150	43.5218
5	700	30	144	43.1672
6	700	35	139	42.8603
7	800	25	159	44.0279
8	800	30	155	43.8066
9	800	35	150	43.5218

Table 7: S/N ratios for hardness values at stir zone.

The plot of main effects for S/N ratios of hardness is as shown in Fig. 6. The plot shows TRS has a significant positive effect on hardness, with S/N ratio increasing as the TRS increases from 600 rpm to 800 rpm. The S/N ratio first decreases from 25 mm/min to 35 mm/min. Derived from the S/N ratio analysis, the best configuration of design variables for maximum hardness is: TRS of 800 rpm and WS of 25 mm/min. This combination yielded the maximum hardness value of 159 VHN in the stir zone. The relationship among TRS and hardness can be explained by thermal effects on the microstructure. Higher rotational speeds and lower feed rate generate higher temperatures and shorter thermal exposure times, which promote dissolution and coarsening of strengthening precipitates in both AA 6061-T6 (Mg_2Si precipitates) and AA 2024-T351 (Al_2Cu precipitates). The stir zone experiences severe thermo mechanical processing that partly dissolves fine precipitates into solid solution. During sudden cooling of the welded specimen, there

may not be sufficient cooling rate to retain a supersaturated solid solution, and the precipitates that form are usually coarser and not so effective enhancement of strengthening compared to the original T6 and T351 temper conditions[19][20].Additionally, higher TRS promotes extensive dynamic recrystallization and extension of grain in the SZ. While moderate grain refinement can increase hardness, excessive heat input and smaller feed rate may lead to grain coarsening, partially keeping aside the strengthening effect of fine grains. It shows that the best combination conditions for maximum UTS and maximum hardness TRS and different WS, indicating challenge in the optimization objectives.

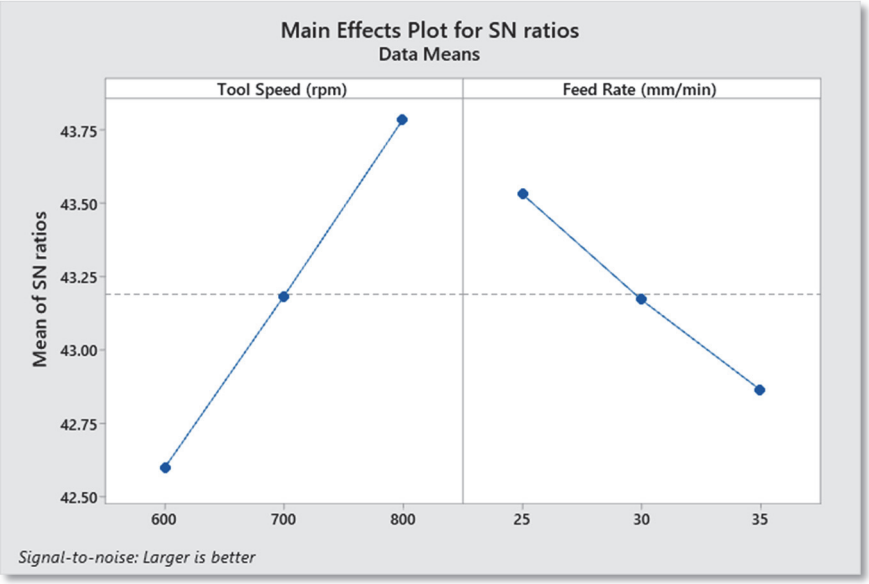

Figure 6: Main effects plot for S/N ratios of hardness values.

Residual analysis for UTS and hardness

To verify the adequacy of statistical model Residual analysis was conducted and also verify the assumptions underlying the analysis. The normal probability plot for UTS and hardness as shown in Fig. 7 and 8 exhibits that the residuals approximately follow a straight line, indicating that the assumption of normally distributed errors is fully satisfied. The residuals versus fitted values plot shows no common pattern indicating constant variance (homoscedasticity) of the residuals across the extent of fitted values. The histogram of residuals indicates near zero symmetric distribution centered. The residuals versus observation order plot indicates no systematic trends, indicating that the independence assumption is met and there are no time-related or sequence-related effects. These diagnostic plots positively confirm that the regression model adequately fits the investigated data and that the statistical inferences drawn from the analysis are valid.

ANOVA for UTS

The ANOVA results for UTS are outlined in Tab. 8. The analysis shows that both TRS and WS are statistically significant factors which affect UTS. TRS contributes 73.87% of the total variation, while WS contributes 21.69%. The error term accounts for only 4.42% of the variation, indicating that the selected parameters adequately explain the observed variability in UTS.

Source	DF	Adj SS	Adj MS	F-Value	P-Value	Cont.(%)
Regression	2	5180.2	2590.08	64.56	0.000	-
TRS (rpm)	1	4004.2	4004.17	99.80	0.001	73.87
WS (mm/min)	1	1176.0	1176.0	29.31	0.002	21.69
Error	6	240.7	40.12	-	-	4.43
Total	8	5420.9	-	-	-	100.0

Table 8: ANOVA results for UTS.

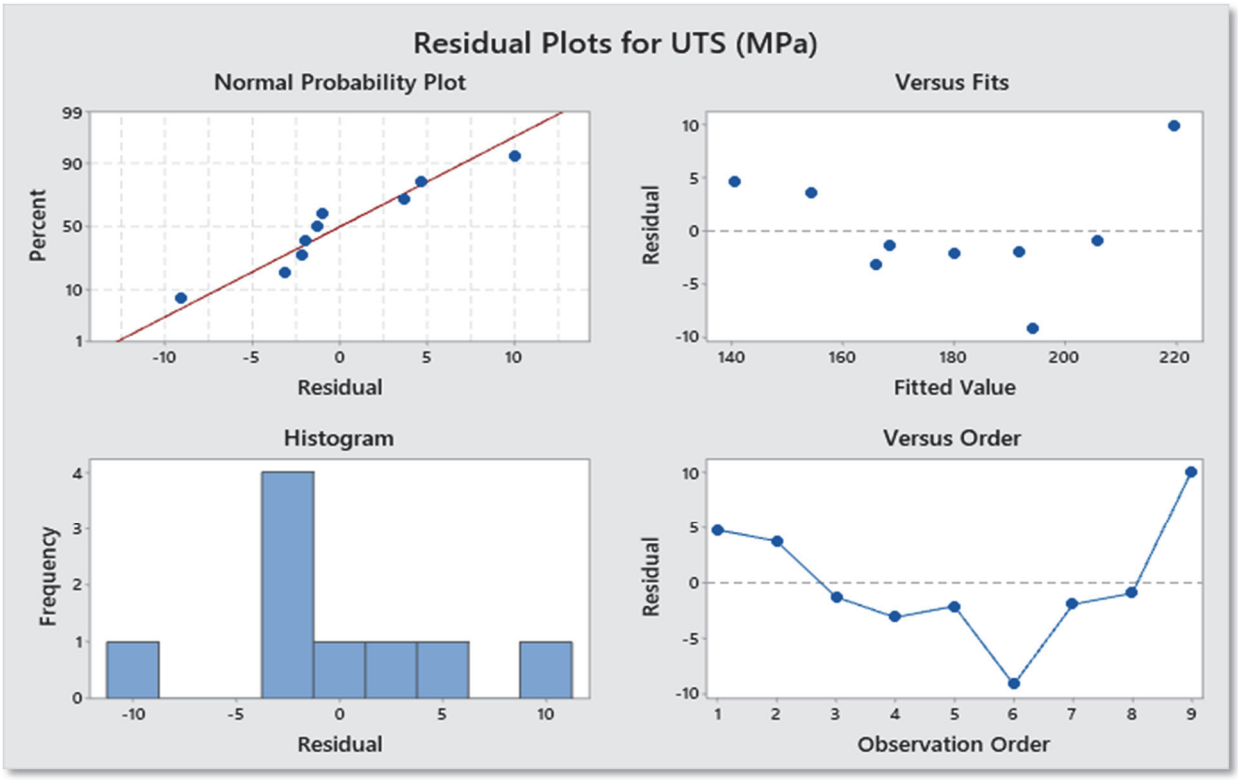

Figure 7: UTS Residual plots.

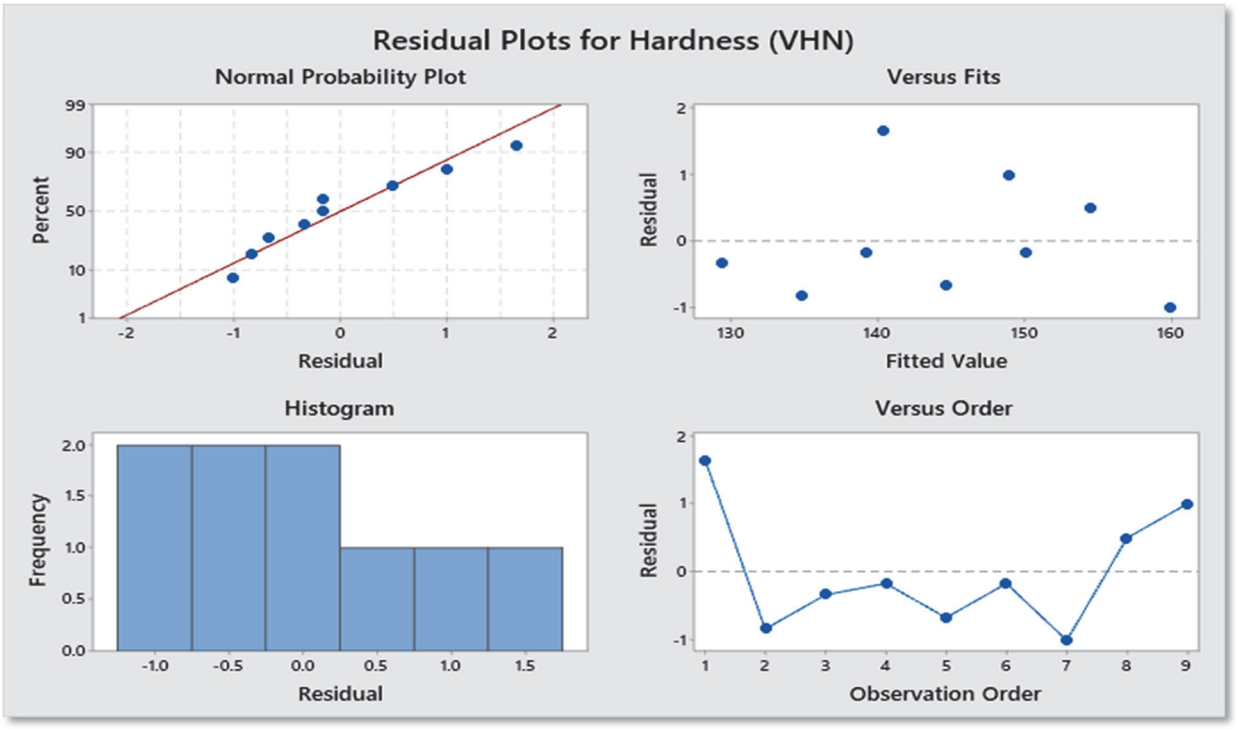

Figure 8: Hardness values Residual plots.

The F-values for TRS is 99.80 and WS is 29.31 are effectively greater than the critical F-value at 95% confidence level confirming their statistical significance. The corresponding P-values are well below the significance level of 0.05, further validating their importance. The TRS emerged as the most influential input parameter, which orients with its substantial effect on thermal gradient and material flow characteristics during the joining. The welding feed rate, while slightly less

influential, still plays an vital role in deciding the heat cycle and mechanical properties of the joint. The high percentage contributions of the selected parameters and low error percentage validate the experimental design and indicate that other uncontrolled factors have minimal impact on the ultimate tensile strength within the experimental conditions conducted.

ANOVA for hardness

The ANOVA results for hardness at the SZ are exhibited in Tab. 9. The analysis shows that tool rotational speed contributes 75.52% of the total variation in hardness, making it the dominant factor. Welding feed rate contributes 23.63%, while the error accounts for 0.824% of the variation. The F-value for tool rotational speed (549.63) exceeds the critical value indicating its strong statistical significance. The F-value for welding feed rate (171.95) is also significant at the 95% confidence level, though equal importance with TRS. The lower error percentage compared to UTS suggests that hardness measurements exhibit greater variability, which may be reason to microstructural heterogeneity in the stir zone.

Source	DF	Adj SS	Adj MS	F-Value	P-Value	Cont.(%)
Regression	2	761.667	380.833	360.79	0.001	-
Tool speed (rpm)	1	580.167	580.167	549.63	0.001	75.52
Feed Rate (mm/min)	1	181.500	181500	171.95	0.001	23.63
Error	6	6.33	1.056	-	-	0.824
Total	8	5420.9	-	-	-	100.0

Table 9: ANOVA results for hardness values at stir zone.

Regression equations

Regression equation for UTS (MPa):

$$\text{UTS (MPa)} = -84.7 + 0.2583\ \text{Tool Speed (rpm)} + 2.800\ \text{Feed rate (mm/min)} \quad (1)$$

The regression model for UTS exhibits a coefficient of determination (R^2) of 95.56%, indicating excellent predictive capability. The model confirms a positive correlation between both parameters and tensile strength, indicating that higher rotational speeds and feed rates improve joint strength within the tested values.

Regression equation for hardness (HV):

$$\text{Hardness (HV)} = 108.83 + 0.09833\ \text{Tool Speed (rpm)} - 1.1000\ \text{Feed Rate (mm/min)} \quad (2)$$

The regression model for hardness shows $R^2 = 99.18\%$, providing best predictive accuracy. The negative coefficient for feed rate and positive coefficient for tool speed parameters confirm that effect of tool rotation speed influence is more than that of feed rate for the hardness consistent with the softening due to thermal effects observed in the SZ.

Material flow and microstructural considerations

The mechanical properties of FSW joints are internally linked to the flow of material behavior and outcome of microstructure in the weld zone. During FSW of dissimilar AA 6061-T6 and AA 2024-T351 alloys, complex material flow patterns created due to differences in flow stress, thermal conductivity behavior, and thermo physical properties of the two alloys. AA 2024-T351 exhibits higher flow stress at higher temperatures compared to AA 6061-T6, which influences the material distribution and mixing in the stir zone. Since AA 2024-T351 is kept on the advancing side is because this side experiences more extensive plastic deformation and maximum strain rates, which are favorable for processing the harder material. On retreating side, where AA 6061 is located, experiences comparatively lower deformation, suitable for the softer alloy[21][22].The TTPP used in this study shows superior material flow through multiple mechanisms. The threads create a vertical stirring action that increases mixing of material from different depth levels, while the taper geometry reduces the squeezing force and welding torque. The threaded pin generates a pumping action that draws material upward on the retreating side and, downward on the advancing side improving material consolidation and reducing any void formation. At lower tool rotational speeds (600 rpm), not enough thermal heat cycle generation which

causes to inadequate plasticization of the material, directing to mixing incomplete and arise of potential defects such as lack of bonding or tunnel defects. The tensile strength is compromised due to discontinuities and stress concentration sites created during welding. Contrarily at the optimal higher rotational speed (800 rpm), sufficient frictional heat softens both alloys substantially, allowing complete material intermixing and eliminating any type of bonding defects. The microstructure of the SZ typically contains of fine equiaxed grains formed through continuous dynamic recrystallization (CDRX) under the extensive plastic deformation at higher temperatures. The grain size in the SZ is notably refined compared to the base materials, which contributes to strength enhancement through the Hall-Petch mechanism. However, the dissolution of strengthening precipitates of both alloys partially offsets this benefit, ensuring that stir zone hardness values that are generally lower than the base material's hardness[23][24].The HAZ in heat-treatable aluminium alloys experiences thermal cycle exposure without much significant plastic deformation, leading to precipitate coarsening and over-aging effects. This region often exhibits the lowest hardness across the weld cross-section and it can become the weak section determining location of the joint failure. In some experimental samples, fracture occurred at the HAZ rather than the stir zone, exhibiting that overall joint strength depends not only on stir zone properties but on the characteristics of adjacent regions.

MICROSTRUCTURAL CHARACTERIZATION

Complete microstructural examination was conducted to find out the relationship between input process parameters, microstructure evolution, and mechanical properties. The FSWed joints exhibited distinct microstructural zones characteristic of FSW process: SZ, TMAZ, HAZ, and base material.

Macrostructure analysis

Macro structural examination of the weld cross-sections showed that the characteristic "basin" or "nugget" shape in the SZ, which is typical of FSW welded joints. Fig. 9 presents images of macro structures of selected welded samples showing the effect of input process parameters on weld morphology and material distribution. The macrostructure analysis revealed that increasing tool rotational speed resulted in wider stir zones and good material intermixing. At lower rotational speeds the stir zone appeared narrower with less obvious material flow patterns, indicating very limited plasticization. A vortex like material patterns and homogeneous mixing of both materials created in significantly expended SZ at higher rotational speed as shown in Fig. 10 [25]. No macroscopic defects found in the welded joints such as tunnel voids, kissing bonds, or lack of penetration were observed in any of the samples within the investigated parameter values, validating adequate heat generation and material consolidation.

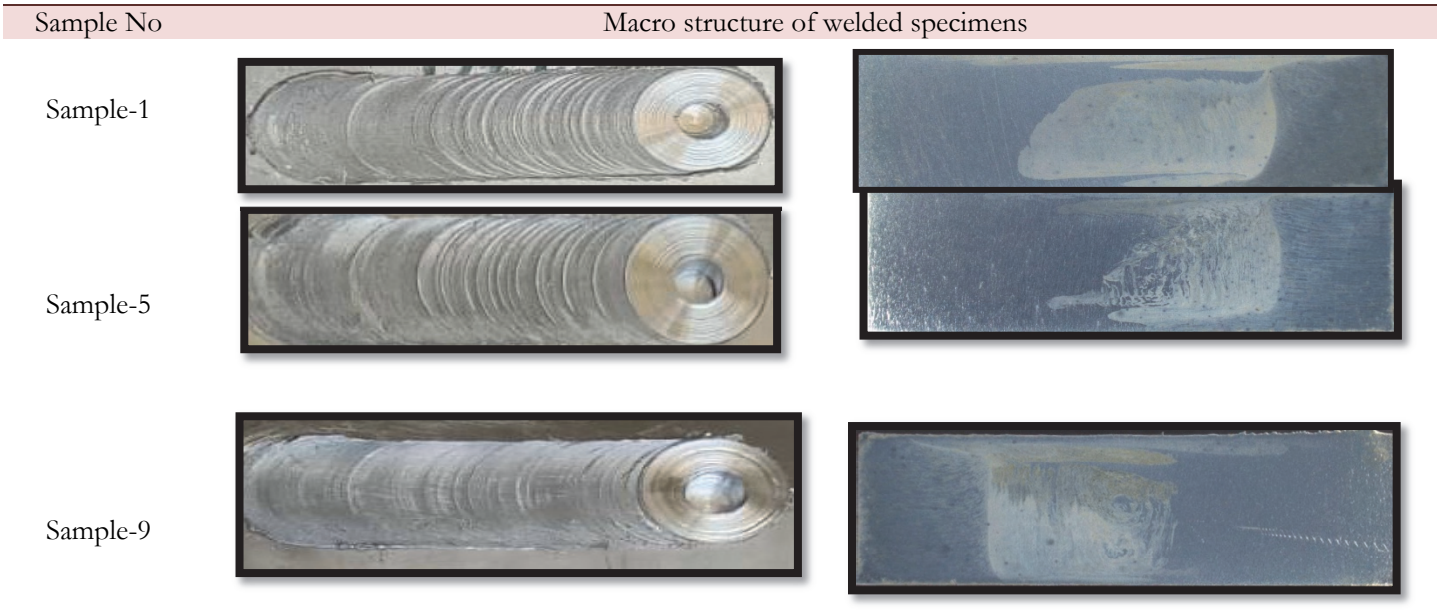

Figure 9: FSW joints Macrostructure (a) Sample 1 (600 rpm, 25 mm/min) - narrow stir zone, (b) Sample 5 (700 rpm, 30 mm/min) - moderate stir zone, (c) Sample 9 (800 rpm, 35 mm/min) - wider stir zone with improved material mixing.

Microstructure of stir zone

As shown in Fig. 10 the stir zone exhibited a fine-grained equiaxed microstructure resulting from continuous dynamic recrystallization (CDRX) during critical plastic deformation at higher temperatures. Sample 9 (800 rpm, 35 mm/min) exhibited a more refined microstructure while Sample 1 (600 rpm, 25 mm/min) showed slightly coarser grains. This grain coarsening at higher rotational speeds is contributed to increased higher temperatures and shorter thermal exposure, which promote grain growth following dynamic recrystallization. The stir zone microstructure showed evidence of precipitate dissolution, particularly at higher rotational speeds. The strengthening precipitates (Mg_2Si in AA 6061-T6 and Al_2Cu-based precipitates in AA 2024-T351) were partially dissolved into solid solution during the FSW thermal cycle. The extent of precipitate dissolution increased with rotational speed, explaining the reduction in stir zone hardness observed at higher heat input conditions.

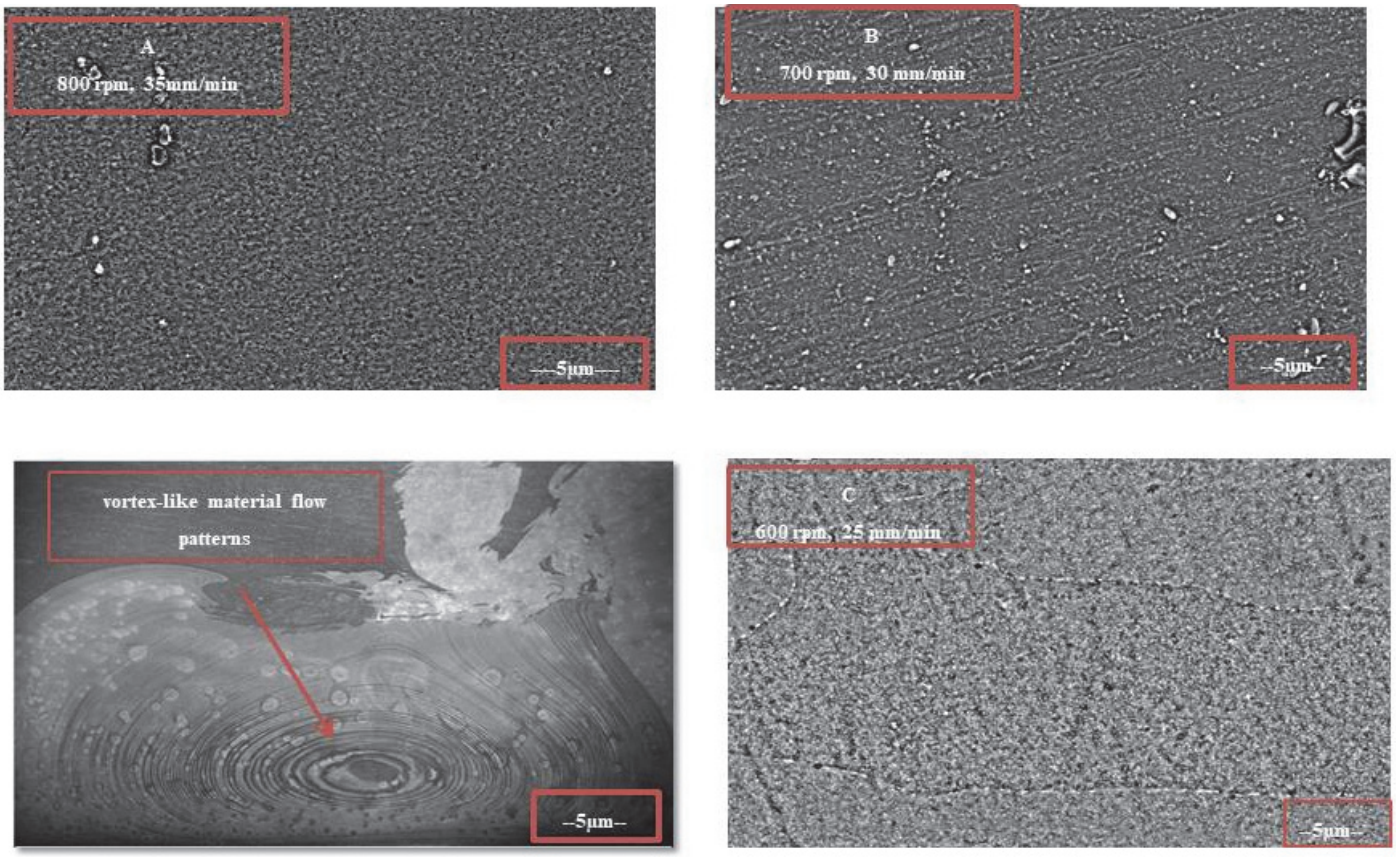

Figure 10: SEM micrographs of stir zone showing (a) Sample 1 (800 rpm, 35 mm/min) - fine equiaxed grains (b) Sample 5 (700 rpm, 30 mm/min) - moderately refined grains (c) Sample 9 (800 rpm, 35 mm/min) - slightly coarser grains with dissolution of precipitates.

Thermo-Mechanically Affected Zone (TMAZ)

The Advancing side (AA 2024) TMAZ, is located adjacent to the SZ of the welded specimen, experiences both thermal cycles and plastic deformation, comparatively though less severe than in the SZ. As shown in Fig. 11 the TMAZ showed elongated and distorted grain structures with evidence of partial recrystallization. On the advancing side (AA 2024-T351), the grains showed more noticeable deformation due to higher strain rates experienced during flow of material around the rotating threaded taper pin. The retreating side (AA 6061-T6) displayed less deformation with visible flow lines indicating material movement toward the stir zone. The width of the TMAZ increased with rotational speed, consistent with the larger thermal cycles at higher heat input conditions. Hardness measurements in the TMAZ revealed intermediate values between the SZ and base material. The TMAZ experiences precipitate coarsening and partial dissolution, reducing its hardness relative to the unaffected base material.

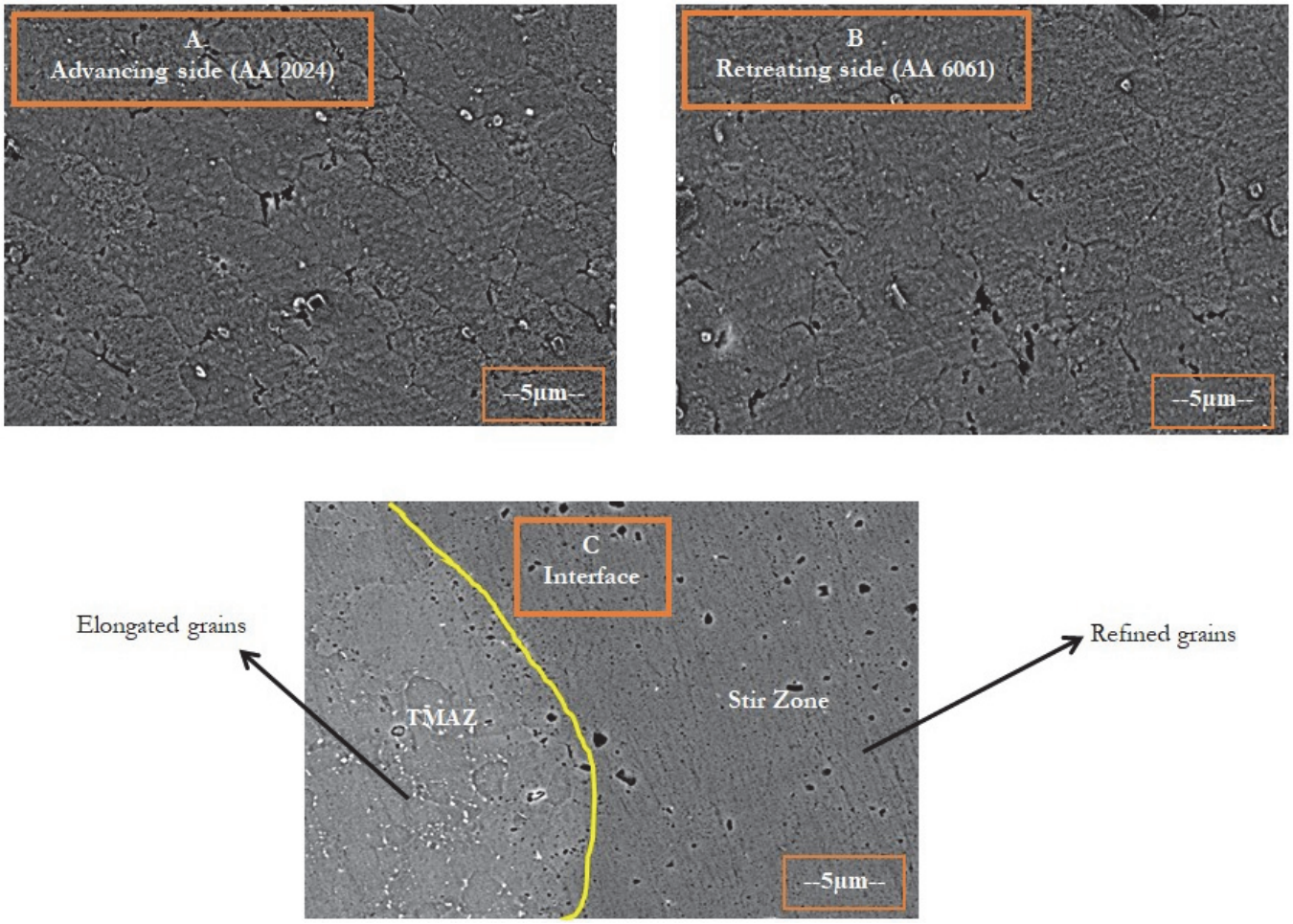

Figure 11: Microstructure of TMAZ showing (a) Advancing side (AA 2024) - elongated and deformed grains with partial recrystallization, (b) Retreating side (AA 6061) - distorted grain structure with flow lines, (c) Interface between TMAZ and stir zone showing transition in grain morphology.

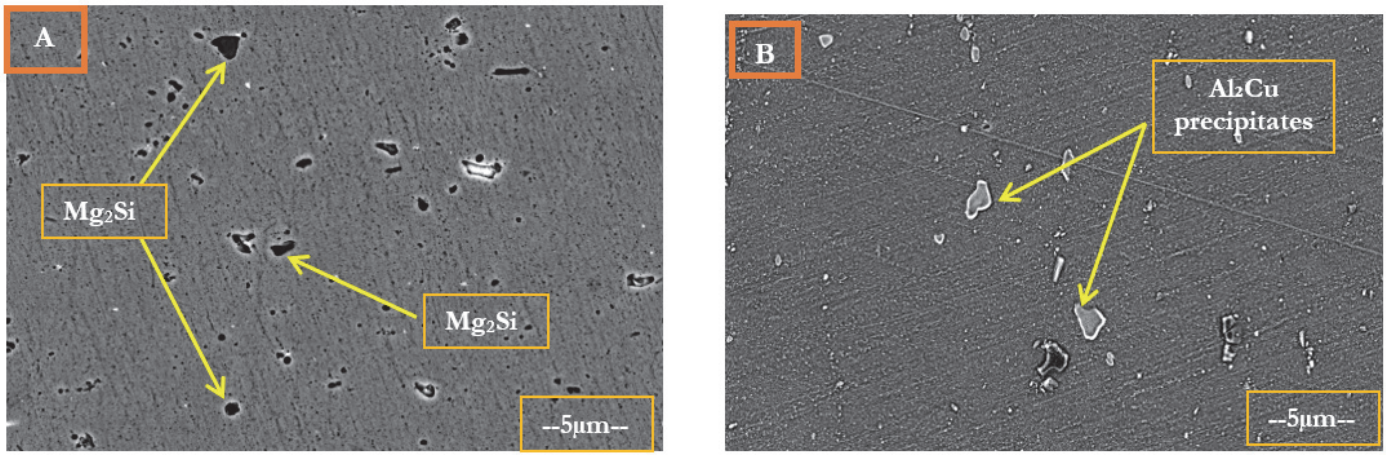

Figure 12: Heat-affected zone microstructure showing (a) HAZ in AA 6061-T6 with coarsened Mg_2Si precipitates, (b) HAZ in AA 2024-T351 with over-aged Al_2Cu precipitates.

Heat-Affected Zone (HAZ)

The HAZ is adjacent to TMAZ which experienced heat cycles without much undergoing plastic deformation, exhibited over-aged microstructures with coarsened precipitates. Fig 12 presents the HAZ microstructure for both base materials. The HAZ exhibited the lowest hardness across the entire weld cross-section, typically 15-25% lower than the base

material hardness. Softening is caused to over-aging and coarsening of strengthening precipitates. The HAZ width increased with increase in TRS due to larger thermal cycles at higher heat input. In several tensile specimens, joint failure has occurred in the HAZ region, especially on the AA 6061 side, confirming that the HAZ often indicates the weakest section in heat-treatable aluminium alloy FSW joints. The grain structure of the HAZ and base metal remained same, with no traces of recrystallization. However, precipitate morphology changed notably, with fine coherent precipitates transforming into coarser in-coherent particles that provide less effective strengthening. This microstructural changes in the HAZ is inherent to FSW of heat-treatable alloys and represents a fundamental challenge in achieving 100% joint efficiencies in welded joints.

FRACTOGRAPHY ANALYSIS

Fractographic investigation of failed tensile specimens was conducted using SEM, to understand the failure mechanisms and their relationship with the process parameters and microstructure. The fracture surfaces provided thoughtful insights about the nature of mechanical bonding, ductility of material, and existance of defect in the welded joints.

Fracture location and mode

Macroscopic examination of failed tensile specimens exhibited that the fracture location was dependent on the welding parameters. Fig. 13 shows the fracture locations for specimens welded at different parameter combinations.

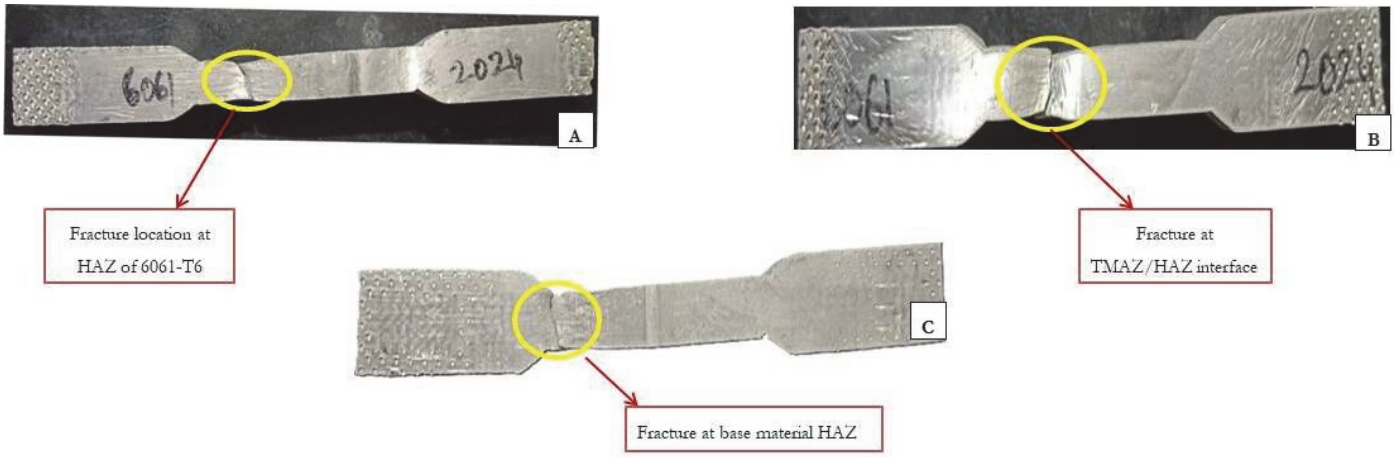

Figure 13: Fracture locations in tensile specimens showing (a) Sample 1 (600 rpm, 25 mm/min) - fracture in HAZ on AA 6061 side, (b) Sample 5 (700 rpm, 30 mm/min) - fracture at TMAZ/HAZ interface, (c) Sample 9 (800 rpm, 35 mm/min) - fracture in base material near HAZ.

For specimens welded at lower rotational speeds (Samples 1-3 of rotational speed 600 rpm), fracture significantly occurred in the HAZ on the AA 6061-T6 side, confirming that this region represents the weakest section in the joint. The HAZ experiences maximum thermal softening by thermal cycles due to precipitate coarsening without compensating benefits of grain refinement or work hardening. At intermediate parameters (Samples 4-6 rotational speed 700 rpm), fracture took place at the interface between the TMAZ and HAZ, showing improved overall joint strength. At the highest rotational speed conditions (Samples 7-9 rotational speed 800 rpm), particularly Sample 9, fracture happened at the base material adjacent to the HAZ, indicating that the weld zone strength approached that of base material. The significant transformation in fracture location from the HAZ zone to the parent base material with increasing TRS shows the advantageous effect of higher thermal input on overall joint integrity, despite the reduction in stir zone hardness. This point confirms the tensile strength results and affirms that joint performance is governed by the weakest section zone of welded joints rather than the stir zone properties alone.

Fracture surface characteristics at low heat input

As shown in Fig. 14 SEM examinations of the fracture surfaces from low heat input conditions revealed a mixed fracture mode with both ductile and brittle nature.

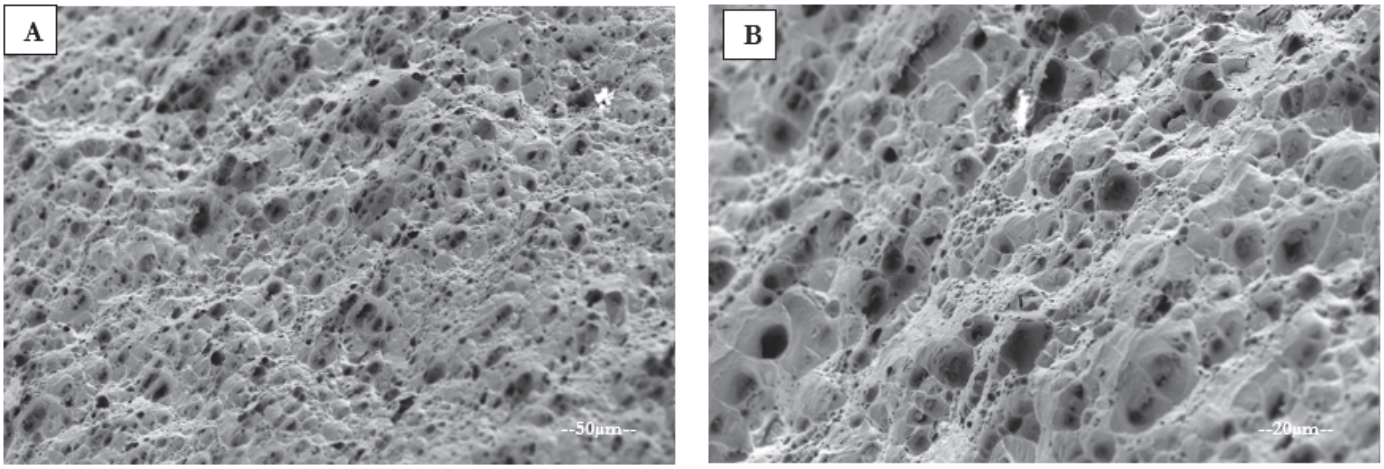

Figure 14: Fracture surface of Sample 1 (600 rpm, 25 mm/min) showing (a) Overall fracture morphology with mixed ductile-brittle features (b) Shallow dimples with indicating limited ductility.

The fracture surface revealed predominantly shallow dimples characteristic nature of limited ductile fracture. Various flat facets and quasi-cleavage features were observed distributed among the dimples, suggesting localized brittle fracture associated with coarsened precipitates in the HAZ. The presence of secondary cracks perpendicular to the main fracture plane indicated limited crack blunting and restricted plastic zone development. Void nucleation sites were primarily connected with 2nd-phase particles and grain boundaries. The comparatively fine dimple structure correlates with the refined grain size and in tensile testing moderate ductility was observed. Some areas showed evidence of incomplete coalescence of micro voids, indicating that fracture propagation involved both void growth and localized shear band formation.

Fracture surface characteristics at intermediate heat input

Fracture surfaces from intermediate parameter conditions (Sample 5: 700 rpm, 30 mm/min) showed enhanced ductile character compared to low heat input conditions. Fig. 15 presents the fractographic features. The fracture surface was dominated by ductile dimples with increased size and depth compared to Sample 1, indicating enhanced plastic deformation morphology. The dimples exhibited equiaxed morphology characteristic of tensile overload failure. Void nucleation was primarily connected with coarse intermetallic particles, with evidence of particle fracture and interfacial de-cohesion. The enlargement in dimple size at intermediate heat input connects with the coarsening of secondary-phase particles and the enhanced ductility resulting from improved material consolidation. The fracture surface showed minimal brittle features, with only occasional flat regions associated with large intermetallic compounds.

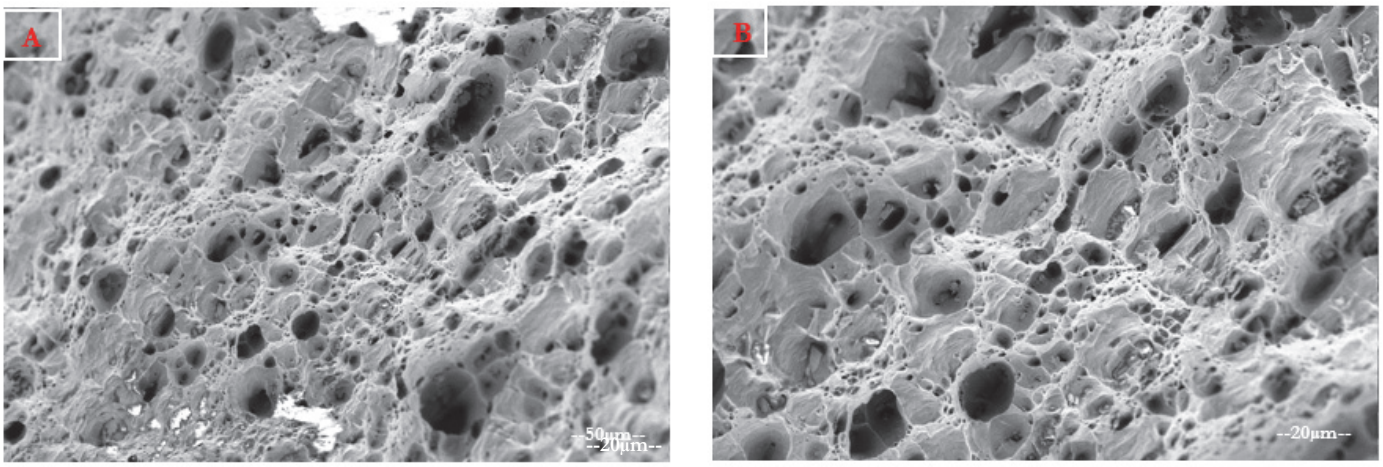

Figure 15: Fracture surface of Sample 5 (700 rpm, 30 mm/min) showing (a) Predominantly ductile dimpled morphology (b) Deep equiaxed dimples

Fracture surface characteristics at high heat input

Specimens welded at the highest heat input conditions (Sample 9: 800 rpm, 35 mm/min) exhibited highly ductile fracture characteristics.

As shown in Fig. 16 the fracture surface displayed fully developed ductile dimple morphology with enlarged, deep dimples. The dimples showed significant variation in its size and shape, with many elongated dimples indicating substantial shear deformation prior to failure. The nature of depth and size of the dimples reflects considerable plastic deformation and high energy absorption during fracture, consistent with the highest UTS of 230 MPa achieved in this investigation. At the center Secondary phase particles were clearly visible of many dimples, confirming their role as void nucleation sites. The particles included both IMC's with some showing evidence of particle cracking. Extensive void coalescence was evident, with elongated ligaments connecting adjacent voids indicating ductile tearing. The fracture surface exhibited extensive tear ridges and no evidence of brittle fracture mechanisms.

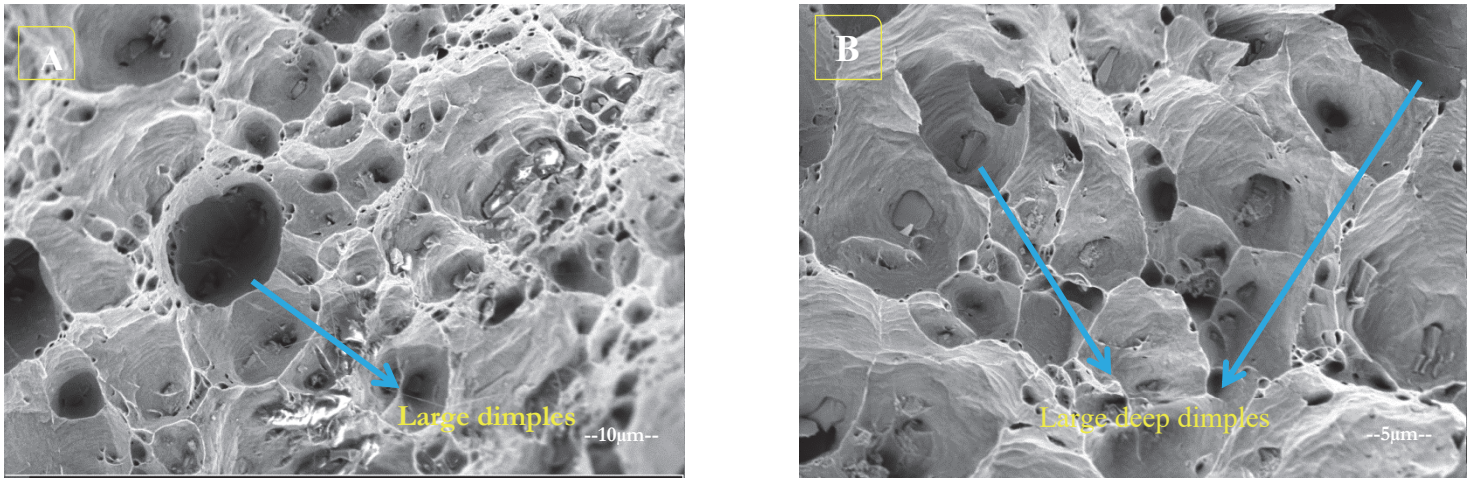

Figure 16: Fracture surface of Sample 9 (800 rpm, 35 mm/min) showing (a) Fully ductile dimpled rupture morphology (b) Large deep dimples indicating excellent ductility.

Effect of process parameters on fracture characteristics

The effects of process parameters to fracture behavior showed clear trend in fractographic analysis: Tool rotation at 600rpm showed shallow dimples which indicate the ductile-brittle nature with limited plastic deformation whereas 700rpm exhibited intermediate dimples and ductile feature with moderate plastic deformation. Highest TRS 800rpm exhibited large deep dimples with fully ductile features and extensive plastic deformation. Improved fracture characteristics were showed at higher feed rates compared to lower feed rates at the same rotational speed. This is associated with reduced thermal exposure preserving some strengthening precipitates while maintaining adequate consolidation.

CONCLUSIONS

This investigation presents a comprehensive statistical evaluation of the mechanical properties of friction stir welded dissimilar aluminium alloys AA 6061-T6 and AA 2024-T351 using a taper threaded pin profile. The Taguchi L9 orthogonal array methodology was successfully employed to optimize process parameters and establish parameter-property relationships. Based on the experimental results and statistical analysis, the following conclusions are drawn:

- By using taper threaded pin profile (TTPP) successfully produced Friction stir welded defect-free joints of dissimilar AA 6061-T6 and AA 2024-T351 alloys across the evaluated parameter range of 600-800 rpm TRS and 25-35 mm/min WS at 0° tilt angle.
- The UTS of the joints varies from 145 MPa to 230 MPa; the highest value was observed at the most stringent conditions (800 rpm and 35 mm/min), suggesting a efficiency of joint roughly 74% when it is compared to the strength of the AA 6061-T6 base material.

- Analysis revealed that TRS was the most significant factor influencing UTS, accounting for 73.87% of the overall variance, while the welding feed rate contributed 21.69%, as established through ANOVA driving better material mixing, dynamic recrystallization, and SZ grain refinement via increased heat input.
- Hardness measurements within the stir zone fluctuated between 129 HV and 159 HV, typically lower than the base material's hardness values, due to the dissolution and coarsening of strengthening precipitates during the heat cycle. Tool rotation speed exhibited a positive correlation with hardness, accounting 75.52% of the total variation. Higher rotational speeds maintained precipitate structures more adequately, resulting in maximum hardness values in the SZ.
- Residual analysis confirms that the accuracy of statistical models (R^2= 95.6% UTS, 99.2% hardness) microstructural analyses (macro/SEM/OM) correlated trends to zone-specific evolution. The residuals showed a normal distribution and consistent variance, which supported the reliability of the optimization results.

REFERENCES

[1] Thomas, W. M., Nicholas, E. D., Needam, J. C., Murch, M. G., Templesmith, P. and Dawes, C. J. (1995). GB Patent Application No. 9125978.8, December 1991 and US Patent No.5460317.

[2] Mishra, R. S. and Ma, Z. Y. (2005). Friction stir welding and processing. Materials Science and Engineering: R: Reports, 50(1-2), pp. 1-78.

[3] Verma, M., Saha, P. and Singh, P.K. (2025). Optimizing heat utilization in dissimilar micro-friction stir welding of AA 2024- T3/AA 6061-T6 using dual backing plate: Impact on local microstructure, mechanical, and corrosion performance, J. Manuf. Process., 149, pp. 98–115. DOI: https://doi.org/10.1016/j.jmapro.2025.05.061.

[4] Sathya, N. N., Herbert, M. A., Shettigar, A. K. and Vatnalmath, M. (2025). Impact of tool rotational speed on friction stir welded joints of AA2014-T6/AA5052-H32: synthesis, microstructural, mechanical and fractographic behaviour, Fract. Struct. Integr., 20(75), pp. 1–12. DOI: https://doi.org/10.3221/IGF-ESIS.75.01

[5] Sadeesh, P., Venkatesh Kannan, M., Rajkumar, V., Avinash, P., Arivazhagan, N., Ramkumar, K. D. and Narayanan, S. (2014). Studies on friction stir welding of AA 2024 and AA 6061 dissimilar metals. Procedia Engineering, 75, pp. 145-149.

[6] Morales, C., Merlin, M., Fortini, A., Garagnani, G. L. and Miranda, A. (2022). Impact behaviour of dissimilar AA2024-T351/7075-T651 FSWed butt-joints: effects of Al2O3-SiC particles addition, *Frat. ed Integrità Strutt.*, 16(60), pp. 504–515. DOI: https://doi.org/10.3221/IGF-ESIS.60.34.

[7] Bahrami, M., Besharati Givi, M. K., Dehghani, K. and Parvin, N. (2014). On the role of pin geometry in microstructure and mechanical properties of AA7075/SiC nano-composite fabricated by friction stir welding technique. Materials & Design, 53, pp. 519-527.

[8] Elangovan, K. and Balasubramanian, V. (2008). Influences of pin profile and rotational speed of the tool on the formation of friction stir processing zone in AA2219 aluminium alloy. Materials Science and Engineering: A, 459(1-2), pp. 7-18.

[9] Taguchi, G., Chowdhury, S. and Wu, Y. (2005). Taguchi's Quality Engineering Handbook. John Wiley & Sons, Hoboken, NJ.

[10] Roy, R. K. (2010). A Primer on the Taguchi Method (2nd ed.). Society of Manufacturing Engineers, Dearborn, MI.

[11] Cavaliere, P., De Santis, A., Panella, F. and Squillace, A. (2009). Effect of welding parameters on mechanical and microstructural properties of dissimilar AA6082-AA2024 joints produced by friction stir welding. Materials & Design, 30(3), pp. 609-616.

[12] Guo, J. F., Chen, H. C., Sun, C. N., Bi, G., Sun, Z. and Wei, J. (2014). Friction stir welding of dissimilar materials between AA6061 and AA7075 Al alloys: Effects of process parameters. Materials & Design, 56, pp. 185-192.

[13] Moradi, M. M., Jamshidi Aval, H. and Jamaati, R. (2016). Experimental investigation on the effect of friction stir welding process parameters in dissimilar joining of AA2024-T351 and AA6061-T6 aluminum alloys. Modares Mechanical Engineering, 16(9), pp. 394-402.

[14] Izadi, H., Fallu, J., Abdel-Gwad, A., Liyanage, T. and Gerlich, A. P. (2013). Analysis of tool geometry in dissimilar Al alloy friction stir welds using optical microscopy and serial sectioning. Science and Technology of Welding and Joining, 18(4), pp. 307-313.

[15] Ma, Z. Y., Mishra, R. S. and Mahoney, M. W. (2002). Superplastic deformation behaviour of friction stir processed 7075Al alloy. Acta Materialia, 50(17), pp. 4419-4430.

[16] Humphreys, F. J., Prangnell, P. B. and Priestner, R. (2001). Fine-grained alloys by thermomechanical processing. Current Opinion in Solid State and Materials Science, 5(1), pp. 15-21.
[17] Fratini, L. and Buffa, G. (2005). CDRX modelling in friction stir welding of aluminium alloys. International Journal of Machine Tools and Manufacture, 45(10), pp. 1188-1194.
[18] Buffa, G., Fratini, L. and Shivpuri, R. (2007). CDRX modelling in friction stir welding of AA7075-T6 aluminum alloy: Analytical approaches. Journal of Materials Processing Technology, 191(1-3), pp. 356-359.
[19] Aval, H. J. (2015). Microstructure and residual stress distributions in friction stir welding of dissimilar aluminum alloys. Materials & Design, 87, pp. 405-413.
[20] Zhang, Z. and Wu, Q. (2015). Numerical studies of tool diameter on strain rates, temperature rises and grain sizes in friction stir welding. Journal of Mechanical Science and Technology, 29(10), pp. 4121-4128.
[21] Khodir, S. A. and Shibayanagi, T. (2008). Friction stir welding of dissimilar AA2024 and AA7075 aluminum alloys. Materials Science and Engineering: B, 148(1-3), pp. 82-87.
[22] Long, T., Tang, W. and Reynolds, A. P. (2007). Process response parameter relationships in aluminium alloy friction stir welds. Science and Technology of Welding and Joining, 12(4), pp. 311-317.
[23] Gaafer, A. M., Mahmoud, T. S. and Mansour, E. H. (2010). Microstructural and mechanical characteristics of AA7020-O Al plates joined by friction stir welding. Materials Science and Engineering: A, 527(27-28), pp. 7424-7429.
[24] Zhang, H. and Liu, H. (2012). Characteristics and formation mechanisms of welding defects in underwater friction stir welded aluminum alloy. Metallography, Microstructure, and Analysis, 1(6), pp. 269-281.
[25] Ouyang, J.H. and Kovacevic, R. (2002). Material Flow and Microstructure in the Friction Stir Butt Welds of the Same and Dissimilar Aluminum Alloy, ASM International Journal of Materials Engineering and Performances 1, pp. 51-63.